JOURNAL OF GEOPHYSICAL RESEARCH, VOL. 106, NO. D10, PAGES 10,349–10,362, MAY 27, 2001

Subgrid variability and stochastic downscaling of modeled clouds: Effects on radiative transfer computations for rainfall retrieval

Daniel Harris and Efi Foufoula-Georgiou

St. Anthony Falls Laboratory, University of Minnesota, Minneapolis, Minnesota

Abstract. The Tropical Rainfall Measuring Mission (TRMM) Microwave Imager (TMI) Goddard Profiling (GPROF) rainfall retrieval algorithm is an inversion type algorithm, which uses numerical cloud models and radiative transfer schemes to simulate the brightness temperatures that the TMI would see, thereby allowing one to relate hydrometeor profiles to brightness temperature. The variability in modeled hydrometeor fields is known to have an important effect on simulated brightness temperatures, and while the TMI instrument sees all the variability down to scales of a few meters, cloud models are typically run at resolutions of 1-3 km. This paper is an illustrative investigation into the importance of subgrid variability (scales below 1-3 km), which is ignored when simulating brightness temperatures. Previous studies on the importance of subgrid variability have been based on comparisons of simulated brightness temperatures computed from hydrometeor fields of a high resolution model and spatially aggregated hydrometeor fields from the same model run. It is argued that numerical cloud models have reduced small-scale variability due to model artifacts such as computational mixing, and this may lead to an underestimation of the importance of including subgrid variability. To address this problem, stochastic downscaling developed in a wavelet-based framework is used to reintroduce the variability reduced by computational mixing. In particular, a high resolution model is spatially aggregated (i.e., upscaled) over the scales affected by computational mixing and stochastically downscaled back to the original resolution of the model. The higher degree of variability introduced by the downscaling (which is a closer approximation to the variability observed in hydrometeor concentrations as compared to that produced by high resolution models) is found to result in larger biases in estimated brightness temperature. This points to the potential for a significant source of bias in microwave-sensed precipitation retrievals that requires further study.

1. Introduction: Background and Problem Statement

1.1. TMI Rainfall Estimation

Estimates of the influence of precipitation processes in the global energy budget of the atmosphere place roughly 75% of the energy as originating from latent heat release in the formation of precipitation. Since almost two thirds of precipitation falls in the tropics and 75% of the tropics are ocean, satellite measurements are necessary to properly estimate the mean and variability of tropical precipitation. This is the justification for NASA's Tropical Rainfall Measuring Mission (TRMM) [e.g., see *Simpson et al.*, 1996].

From a precipitation standpoint, the three principal instruments on the TRMM satellite are (1) the TRMM Microwave Imager (TMI), a passive microwave sensor, (2) the Precipitation Radar (PR), an active microwave transmitter-receiver and the first space-borne precipitation radar, and (3) the Visible and Infrared Sensor (VIRS), a visible-infrared passive radiometer. Only the TMI instrument is addressed in this study.

Paper number 2000JD900797.
0148-0227/01/2000JD900797$09.00

The TMI Rainfall Algorithm, often referred to as 2A12 or the Goddard Profiling Algorithm (GPROF), is an inversion type algorithm, which, in short, amounts to using numerical cloud models and radiative transfer schemes to simulate the brightness temperatures that the TMI would see, thereby allowing one to relate hydrometeor profiles to brightness temperature. These inversion algorithms have been in use to retrieve rainfall from Special Sensor Microwave Imager (SSM/I) measured brightness temperatures. Recent references for the inversion type algorithm discussed here include *Kummerow et al.* [1996] and *Panegrossi et al.* [1998]. Earlier references include work by *Kummerow and Giglio* [1994], *Smith et al.* [1994], and *Mugnai et al.* [1993].

The numerical cloud models are typically run at resolutions varying from 1 to 3.3 km [e.g., *Panegrossi et al.*, 1998] and are used to simulate different types of rain and their corresponding hydrometeor profiles. The hydrometeors considered here explicitly fall into six categories: (1) non-precipitating water (i.e., cloud liquid water (CLW)), (2) nonprecipitating ice (i.e., cloud ice water (CIW)), (3) precip-itating water or rain liquid water (RLW), (4) precipitating ice (i.e., hail, graupel), (5) snow, and (6) water vapor. Water vapor is not a hydrometeor but interacts with microwave radiation and so is grouped in with the other five species of hydrometeors for convenience. Oxygen is also radiometric-ally significant but is not considered explicitly in the cloud model but rather dealt

with implicitly in the radiative transfer scheme. The hydrometeor profiles are represented in the model as volume averaged densities (measured in g m^{-3}) of the six types of hydrometeor species at a number of levels, N_z, in the vertical.

The TMI observed microwave radiance results from the vertically integrated effects of microwave interaction (absorption, emission, and scattering) with the hydrometeors. The observed radiance is also dependent on (1) the vertical atmospheric temperature profile, (2) the emissivity and temperature of the surface, and (3) the nature of the surface defined as either specular or Lambertian. It is convenient to explicitly define a complete state vector referred to here, in accordance with previous notation found in the literature [*Kummerow et al.*, 1996], as $\mathbf{R}(x, y)$. This state vector represents, at any horizontal coordinate (x, y), the hydrometeor densities and the atmospheric temperatures at all N_z vertical levels, as well as the surface characteristics. The state vector is thus used, together with a radiative transfer scheme, to determine the radiance the TMI would see when looking at the modeled atmosphere. Note that for any (x, y) coordinate, the state vector, $\mathbf{R}(x, y)$, will consist of $7N_z$ values ($6N_z$ for the hydrometeor species and $1N_z$ for vertical temperature profile) plus the three surface characteristics (emissivity, temperature, and whether the surface is specular or not).

Many cloud models have been used for inversion scheme studies. The principal cloud model used for the 2A12 NASA-TRMM TMI rainfall product is the Goddard Cumulus Ensemble (GCE) model [*Tao and Simpson*, 1993]. *Panegrossi et al.* [1998] used models such as the University of Wisconsin Nonhydrostatic Modeling System (UW-NMS) and the Wisconsin Dynamical-Microphysical Model (WISCDYMM) with Hail Parameterization Model (HPM). In this study we use the Advanced Regional Prediction System (ARPS) developed at the Center for the Analysis and Prediction of Storms (CAPS), University of Oklahoma. The model features a similar microphysical scheme (see *Lin et al.* [1983] for a detailed description) and parameterization to that used in the GCE model.

To simulate what the TMI instrument would see while looking through the modeled atmosphere, radiative transfer schemes are run through the cloud models to obtain simulated brightness temperatures, $\mathbf{T}_{\mathbf{b},\mathrm{sim}}$, at the model resolution. The $\mathbf{T}_{\mathbf{b},\mathrm{sim}}$ and $\mathbf{R}$ fields are then averaged to the "measurement resolution" (~10-20 km; see *Kummerow et al.* [1998] for details on TMI resolution), thus creating a large database of $(\mathbf{T}_{\mathbf{b},\mathrm{sim}}, \mathbf{R})$ pairs at this measurement resolution. To be accurate, it is noted that the measurement resolution referred to in this study is not the physical footprint of the sensor. The footprint is larger but the footprints overlap, and through the use of deconvolution techniques [*Farrar et al.*, 1994], information at a resolution higher than the footprint may be retrieved. It is also important to note that the instrument averages horizontally over the footprint in $\mathbf{T}_\mathbf{b}$ rather than $\mathbf{R}$. More precisely, the instrument actually averages the radiance over its angle of view. However, one can show with a simple plot of $\mathbf{T}_\mathbf{b}$ versus radiance that the relation between $\mathbf{T}_\mathbf{b}$ and radiance (Planck's law of radiation) is linear to an excellent degree of approximation for the TMI channel frequencies and the range of $\mathbf{T}_\mathbf{b}$ and radiance observed.

The final step of the rainfall retrieval involves "matching" the simulated $\mathbf{T}_{\mathbf{b},\mathrm{sim}}$ with the TMI observed brightness temperatures, $\mathbf{T}_{\mathbf{b},\mathrm{obs}}$. This is accomplished within a Bayesian framework [e.g., *Kummerow et al.*, 1996], where the large database of $(\mathbf{T}_{\mathbf{b},\mathrm{sim}}, \mathbf{R})$ pairs represents a realistic sampling of the "flavors" of rain likely to occur in the tropics. Discussion of this final step is beyond the scope of this paper.

1.2. Problem Statement

This study is concerned with scale and variability issues in the TMI rainfall estimation process described in section 1.1. The process involves a number of scales, which are schematically illustrated in Figure 1. First, there is the scale associated with the pixel size of the $(\mathbf{T}_{\mathbf{b},\mathrm{sim}}, \mathbf{R})$ database, which is chosen to correspond to the TMI "measurement resolution" of the order of 10-20 km. Second, there is the scale associated with the pixel size of the cloud model, which is typically between 1 and 3 km. The variability in the cloud fields for all scales below the typical model resolutions of 1-3 km is referred to here as the "subgrid variability." We refer to "small-scale variability" as the variability between the model resolution and the TMI measurement resolution. One must also acknowledge the real physical process scale down to the order of meters, which the real instrument "sees" as it integrates over its footprint, yet which the model does not resolve. As mentioned above, the $(\mathbf{T}_{\mathbf{b},\mathrm{sim}}, \mathbf{R})$ pairs in the database are results of $\mathbf{T}_{\mathbf{b},\mathrm{sim}}$ and $\mathbf{R}$ computed at the model resolution then averaged to the TMI measurement resolution for the purposes of the database. However, $\mathbf{T}_{\mathbf{b},\mathrm{sim}}$ and $\mathbf{R}$ are non-linearly related. Therefore differences in the fine scale variability of the $\mathbf{R}$ field from which $\mathbf{T}_{\mathbf{b},\mathrm{sim}}$ is computed lead to differences in the computed $(\mathbf{T}_{\mathbf{b},\mathrm{sim}}, \mathbf{R})$ relations, even though the coarse resolution (i.e., 10-20 km) $\mathbf{R}$ field may remain unchanged. Part of this variability is the subgrid variability. The question motivating this study is therefore: Does including variability at scales < 3 km affect $\mathbf{T}_{\mathbf{b},\mathrm{sim}}$ estimates and if so, by how much?

A simple numerical experiment to answer this question involves running a cloud model at a resolution much higher than 3 km (375 m was used in this study). Then one can compare $\mathbf{T}_{\mathbf{b},\mathrm{sim}}$ computed at 375 m resolution with that computed at 3 km resolution by spatially aggregating the 375 m hydrometeor fields prior to applying the radiative transfer schemes. However, such a comparison does not fully address the question since it is argued that the model-produced clouds have significantly reduced variability compared to observed clouds for scales between the model resolution and 8 times

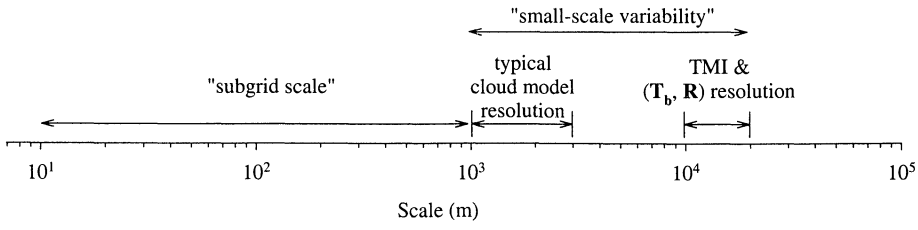

Figure 1. Schematic illustration of scales.

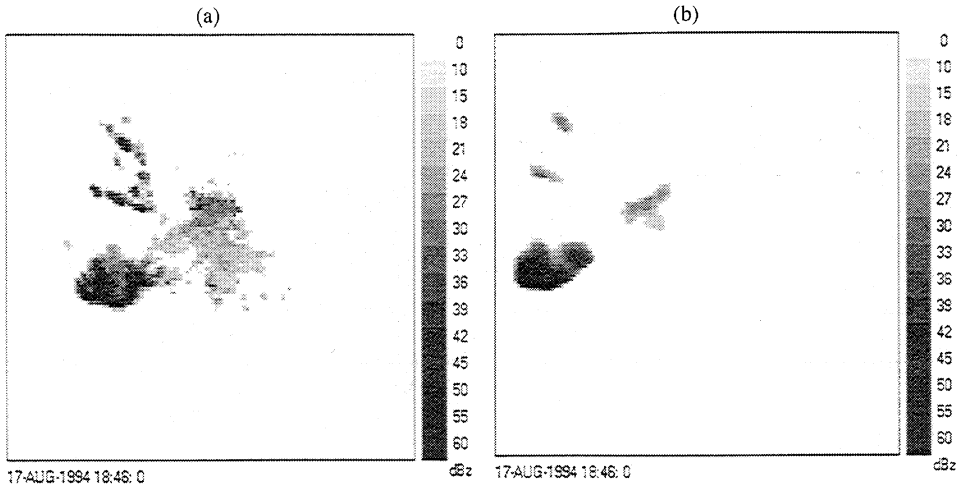

Figure 2. Visual comparison of reflectivity fields of (a) radar observations of a supercell at 2 km resolution and (b) an Advanced Regional Prediction System (ARPS) model representation of the same storm at 3 km resolution. While the radar observations comprise more low level signals (which may even be due to clutter and other radar artifacts), the variability of the intense features of the storm appears greater for the radar observation than for the modeled field.

this scale (i.e., 375 m to 3 km in our case). We therefore propose that an adequate investigation into the importance of subgrid variability requires that this variability be properly represented in the first place. A way of accomplishing this is proposed in this study and is used to enhance the modeled cloud variability to better match the observed subgrid variability of clouds.

One of the mechanisms which contributes to the smoothness observed in modeled fields is the process of computational mixing or numerical smoothing. This is an artificial process necessary, in some form or another, for finite difference computational fluid dynamical (CFD) models. While computational mixing is designed to remove small-scale computational noise and ensure computational stability, it also reduces small-scale variability of dynamic and scalar fields.

By a simple visual comparison one finds that modeled precipitation tends to look smoother and less variable than precipitation observed with a radar. For example, Figure 2 shows a comparison of radar observed reflectivity fields of a supercell storm and an ARPS model representation of that same storm made using a wide variety of assimilated data. By most meteorological standards the modeled field would be considered a very good forecast, since for forecast purposes the small-scale variability would be largely unimportant. However, for radiative transfer computations it may well be important because of the non-linear relation between $\mathbf{T_b}$ and hydrometeor concentrations. In essence, this is known as the beam-filling problem [e.g., *Kummerow*, 1998; *Kummerow et al.*, 1996; *Kummerow and Giglio*, 1994; *Spencer*, 1986], which is largely a problem of non-linear averaging of precipitation. With respect to our objective of examining the effect of subgrid variability on $\mathbf{T_{b,sim}}$ estimates, our concern is that if the modeled subgrid variability is underrepresented because of computational mixing, one may be misled as to the importance of accounting for it.

To address this concern, the following approach is therefore undertaken in this study. A cloud model is run at a very high resolution of 375 m. Radiative transfer computations performed at this resolution can thus be compared with radiative transfer computations performed on a cloud model at a resolution of 3 km (obtained by simply horizontal spatial averaging of the 375 m model). This alone gives an estimate of the degree of importance of including subgrid variability in $\mathbf{T_{b,sim}}$ estimation and is similar to the approach followed by *Haferman et al.* [1994] but done here for higher resolutions. However, to alleviate the problem of underrepresented variability in the 375 m model run (i.e., variability between scales of 375 m to 3 km), we upscale the model output to 3 km and apply recently developed wavelet-based methods [e.g., *Perica and Foufoula-Georgiou*, 1996b] to stochastically downscale the 3 km aggregated fields back to 375 m resolution. This procedure increases the subgrid variability relative to that of the original modeled field to better match the observed variability and we argue that it results in a better estimate of the importance of including subgrid variability in $\mathbf{T_{b,sim}}$ computations.

The horizontal variability of hydrometeor concentrations in precipitating clouds is expected to have important effects on the upwelling brightness temperature, particularly where scattering is dominant [*Stephens*, 1989]. This effect, dependent on the modeling of the horizontal component of radiative transport, clearly requires three-dimensional (3-D) radiative transfer schemes [*Haferman et al.*, 1994; *Roberti et al.*, 1994] as opposed to plane-parallel independent pixel approximations of the radiative transfer equations. While applying a 3-D radiative transfer scheme is more desirable, a first-order measure of the beam-filling problem can be achieved [e.g., see discussion by *Haferman et al.*, 1994] using a plane-parallel or Independent Column Approximation (ICA) radiative transfer scheme. This study uses an ICA radiative transfer scheme and thus can be seen as a first step in addressing the importance of subgrid variability to the beam-filling problem. More importantly the study assesses the benefits of introducing stochastic downscaling methods to address issues of inadequate precipitation variability in numerical cloud models. A more elaborate 3-D radiative transfer analysis in conjunction with a

3-D downscaled cloud representation (which requires a detailed parameterization of the vertical structure of hydrometeors) is currently under investigation.

2. Cloud Model and Radiative Transfer Scheme

The model used here is the Advanced Regional Prediction System (ARPS) developed at the Center for the Analysis and Prediction of Storms (CAPS) at the University of Oklahoma. As the name suggests, ARPS is more than a cloud model (it is a system) and incorporates many advances in data assimilation developed at CAPS. Its aim is operational severe storm forecasting, and it is currently providing real-time forecasts at horizontal resolutions as high as 3 km (for examples on-line, visit http://caps.ou.edu/wx/aa). For the purposes of this work, however, the model was run at a very high resolution of 375 m in the horizontal in order to explore the effects pertaining to the contribution of subgrid variability (i.e., scales below 3 km). This was done on a square domain of 160×160 km in size.

Details of the ARPS model are given by *Xue et al.* [1995] (on-line at http://caps.ou.edu/ARPS/ARPS4.guide.html). As is for most cloud models, ARPS is physically based and operates on finite difference representations of the Navier-Stokes equations as well as thermodynamic and microphysical processes. One might thus expect such cloud models to exactly reproduce the variability found in observed fields. However, this is often not so over the full range of modeled scales as many of the subgrid processes, such as turbulent dissipation, for example, must necessarily be parameterized. This continues to be an active area of research [e.g., *Porté-Agel et al.*, 2000, 2001]. Also, like the real atmosphere, the models are chaotic and sensitive to perturbations, which for a model may be brought on by numerical noise. Thus care must be taken to dampen the effects of any numerical noise by a process often referred to as computational mixing. Computational mixing ensures computational stability, and is usually the only purely nonphysical process in any computational fluid dynamical model. This mixing acts on dynamical as well as scalar fields and as a general rule of thumb is expected to have some effect on the variability of these fields at scales up to $6\Delta x$ to $8\Delta x$, where Δx is the model horizontal resolution. Notice that $8\Delta x$, for Δx = 375 m is equal to 3 km and is thus the reason for choosing a resolution of 375 m for the high resolution run. Choosing this resolution means that at scales of 3 km the modeled variability should be largely unaffected by computational mixing.

The ARPS model run generated here used a fourth-order mixing scheme which, in a nutshell, adds to the principal conservation equations, a small term proportional to the fourth-order partial derivatives of the perturbation of a field quantity, from its base state or, say, initial value. The proportionality constants (there are two: one for the horizontal, K_h, and one for the vertical, K_v) in this additive term are the mixing coefficients, sometimes referred to as the computational diffusion coefficients [e.g., *Pielke*, 1984; *Xue et al.*, 1995]. The values for the fourth-order order mixing coefficients used in this study were $K_h = 2\times10^7$ m^4 s^{-1} and $K_v = 2.5\times10^7$ m^4 s^{-1}.

The model run for this work is simplified in that it has no real data assimilated in the initial field and represents an intense storm triggered in an environment of high instability quantified by the convective available potential energy (CAPE). The environment is initialized with an analytic sounding [*Weisman and Klemp*, 1982] plus the addition of helicity [*Droegemeier et al.*, 1993]. Also, for the purposes of this work, surface parameterizations were not included, and radiative effects were neglected. Of relevance to this work, of course, is the microphysical parameterization scheme [*Lin et al.*, 1983], which is similar to that used in the GCE model and features cold rain microphysics.

The Eddington ICA radiative transfer scheme used by *Kummerow* [1993] was used for this study. This scheme was chosen because it was well documented, and readily available with kind support from the author [*Kummerow*, 1993]. One must keep in mind that use of an Independent Column Approximation has the shortcoming of not accounting for 3-D radiative effects, in contrast to some of the later schemes such as the 3-D Monte Carlo [*Roberti et al.*, 1994; *Roberti and Kummerow*, 1999] and 3-D Discrete Ordinates Method [*Haferman et al.*, 1994]. However, as discussed in section 1, use of an Independent Column Approximation suffices for the purpose of illustrating the importance of adequately representing subgrid variability for radiative transfer computations.

In the radiative transfer scheme the viewing zenith angle was 50° from nadir, and some simplifications were made. First, all ice species were grouped together (i.e., cloud ice grouped together with precipitating ice and snow) as a single ice species. Second, the surface characteristics were fixed and set to represent a nonspecular sea surface (i.e., Lambertian), with an emissivity of 0.5 and a surface temperature equal to the atmospheric air temperature at ground level (typically 295° to 300°K).

3. Fourier Power Spectrum and Scaling in Atmospheric Fields

A simple yet conceptually powerful tool for looking at the variability of any field over a wide range of scales is the Fourier power spectrum. The power spectrum is computed using standard fast Fourier transform (FFT) algorithms such as those given by *Press et al.* [1992]. An empirical observation often (but not always) noted for a wide variety of atmospheric fields is the presence of scaling or scale-invariance, which manifests itself as log-log linearity of the power spectrum in space or time. Evidence of scaling power spectra for rain fields in both space and time can be found in numerous studies [e.g., *Harris et al.*, 1996; *Menabde et al.*, 1997; *Lovejoy and Schertzer*, 1995; *Georgakakos et al.*, 1994] as well as for cloud liquid water fields [e.g., *Davis et al.*, 1996; *Lovejoy and Schertzer*, 1995]. The scaling nature of these atmospheric fields is largely empirical, although there are arguments in the literature suggesting that the scaling of observed scalars such as rainwater or cloud water is linked to the scaling observed in turbulence [*Schertzer and Lovejoy*, 1991].

As discussed in section 2, computational mixing influences the variability over a range of scales from the horizontal model resolution, Δx, up to $6\Delta x$ to $8\Delta x$ and this should be reflected in the tails of the power spectra of modeled scalar and dynamical fields. Indeed, comparisons of power spectra show a steeper falloff for modeled rainwater and cloud water fields than for observed fields. For example, Figure 3a shows the spectrum for modeled cloud liquid water (CLW). The spectrum was computed from horizontal transects of CLW from a continental squall line modeled at 1 km resolution. The spectrum shown is an average of several transects in order to reduce noise. For comparison, the dashed line represents the

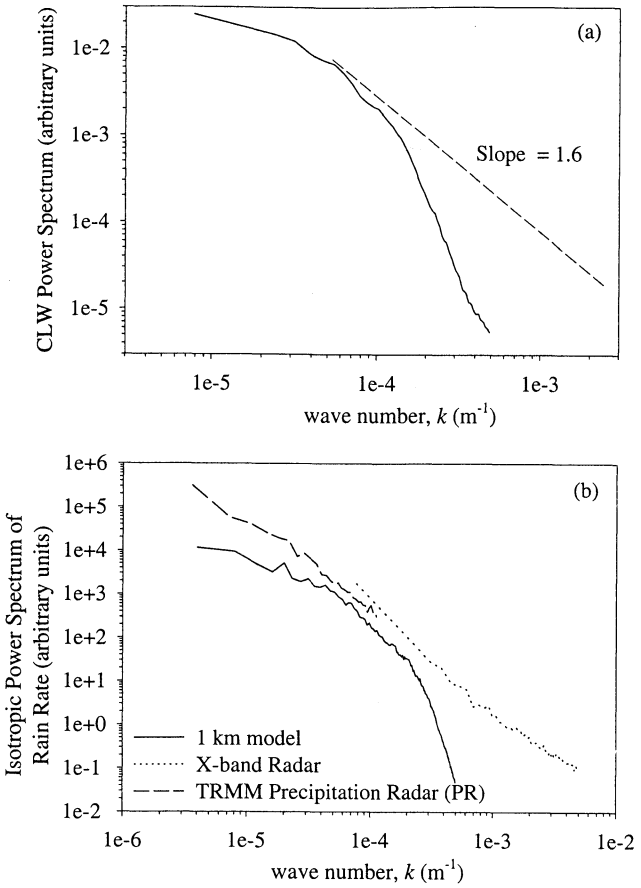

Figure 3. Fourier power spectra for observed and modeled fields of (a) cloud liquid water (CLW) and (b) rain rate. The CLW spectrum of the model is computed from horizontal transects obtained from a 1 km model run. The dashed line has a slope of 1.6 as found for in situ CLW measurements by *Davis et al.* [1996]. Rain rate spectra are for modeled and radar observed fields.

mean spectral slope given by *Davis et al.* [1996] for CLW measurements made with a variety of liquid water probes flown through marine stratocumulus clouds. This type of scaling is reported to extend down to scales of tens of meters. While the modeled cloud field from which the spectrum is computed is not marine stratocumulus (i.e., the model features deep convection), the spectrum falloff even for convective clouds is not expected to be anywhere as steep as that shown in Figure 3a.

Similarly for rain fields, Figure 3b shows a spectral comparison between observed and modeled fields for 2-D rain rate maps of the same model run used for Figure 3a. (Details on the representation of 2-D Fourier power spectra are given in Appendix A.) The spectrum of the modeled rain rates is found again to drop off quicker than for the observations provided by TRMM PR (i.e., 2A25 product) for a storm occurring during the Texas and Florida Underflights-A (TEFLUN-A) ground validation observation period and data from a high resolution scanning X-band radar [*Seed et al.*, 1996] having 100 m resolution.

In both cases of modeled CLW and rain rates the steep falloff at high wave numbers (small scales) is indicative of a smoother structure and reduced variability in comparison to their observed counterparts. Further documentation of the discrepancies between the multiscale structure of modeled and observed clouds is given by D. Harris et al. (Multiscale statistical properties of a high resolution precipitation forecast, submitted to *Journal of Hydrometeorology,* 2000).

4. Wavelet Decomposition, Normalized Fluctuations and Stochastic Downscaling

4.1. Wavelet Decomposition and Normalized Fluctuations

A more descriptive multiscale analysis tool involves the wavelet decomposition of signals [e.g., *Daubechies*, 1992], which has recently found applications in the study of numerous geophysical processes [e.g., see *Foufoula-Georgiou and Kumar*, 1994]. The details of the method described in this section are well documented in a number of publications [e.g., see *Perica and Foufoula-Georgiou*, 1996a, 1996b; *Kumar and Foufoula-Georgiou*, 1993a, 1993b], and the reader is referred to those. Below, only a brief description is given for completeness, and attention is paid to the physical interpretation of the quantities that the analysis method yields.

Using the Haar wavelet, ψ, and the corresponding scaling function, ϕ, an illustration of a discrete orthogonal wavelet decomposition is given for a time series in Figure 4. In essence, if one is using the Haar wavelet (there is a large suite of wavelets one can choose from, but only the Haar wavelet is used here), the corresponding scaling function acts as a simple local averaging of the time series (reducing the resolution of the time series by a factor of 2 at each step), while the wavelet transform records the "details" or fluctuations around the local means. An important property of a discrete orthogonal wavelet decomposition is that the decomposition process is entirely reversible (by an inverse wavelet transform), and the original time series in Figure 4 may be recreated by the average at a large scale and its "details" at all intermediate scales. On the basis of the empirical evidence of *Perica and Foufoula-Georgiou* [1996a] the details, or fluctuations, X', of the rainfall process at any scale depend almost linearly on the average rainfall intensities, $\overline{X}$, at that same scale. We therefore analyze the normalized quantity, $\xi = X'/\overline{X}$ [*Perica and Foufoula-Georgiou*, 1996a] at each successive iterative step of the decomposition. For the Haar wavelet the quantities ξ, at each scale, are simply interpreted as normalized local rainfall fluctuations.

For spatial data a 2-D separable Haar wavelet [e.g., *Kumar and Foufoula-Georgiou*, 1993b] is used which results in three separate wavelet components. These represent fluctuations in the longitudinal, latitudinal, and diagonal directions. Again, by using the Haar wavelet transform these can be simply represented by the set of equations

$$X'_{m+1,1}(i',j') = \frac{1}{4}\{[\overline{X}_m(i,j) + \overline{X}_m(i,j+1)] - [\overline{X}_m(i+1,j) + \overline{X}_m(i+1,j+1)]\}$$

$$X'_{m+1,2}(i',j') = \frac{1}{4}\{[\overline{X}_m(i,j) + \overline{X}_m(i+1,j)] - [\overline{X}_m(i,j+1) + \overline{X}_m(i+1,j+1)]\}$$

$$X'_{m+1,3}(i',j') = \frac{1}{4}\{[\overline{X}_m(i,j) - \overline{X}_m(i+1,j)] - [\overline{X}_m(i,j+1) - \overline{X}_m(i+1,j+1)]\}$$

$$\overline{X}_{m+1}(i',j') = \frac{1}{4}\{\overline{X}_m(i,j) + \overline{X}_m(i;j+1) + \overline{X}_m(i+1,j) + \overline{X}_m(i+1,j+1)\} \quad , m = 0,1,2\ldots \quad (1)$$

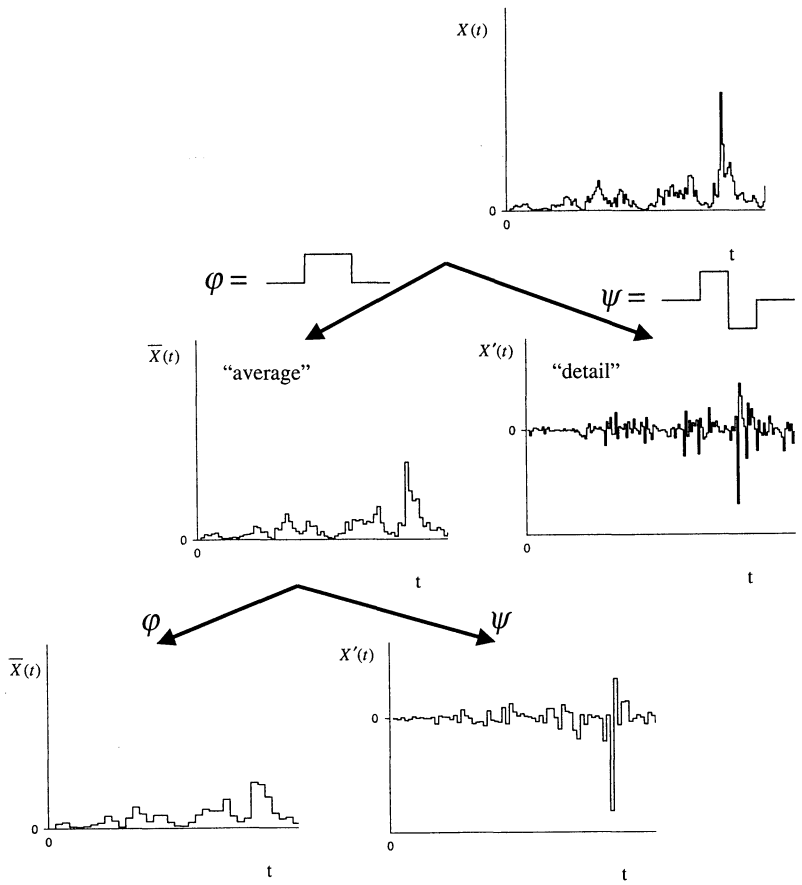

Figure 4. Schematic of iterative discrete Haar wavelet decomposition for a rainfall time series. The original field $X(t)$ is decomposed into an averaged field, $\overline{X}(t)$ (via filter φ) and a difference field $X'(t)$ (via filter ψ). The averaged field, $\overline{X}(t)$, is further decomposed at the next iteration, and so on, until the desired coarse scale is obtained. Since the decomposition is orthogonal, the original field can be reconstructed from the averaged field at any scale and the difference fields at all intermediate scales.

The index, m, indicates the iteration (scale of decomposition) and the indices, i and j, represent the row and column indices, respectively, of the 2-D field. Note that $m = 0$ corresponds to the original scale of 375 m, and the first decomposition yields normalized fluctuations at the 750 m scale; $m = 1$ corresponds to the scale of 750 m, and the second decomposition yields normalized fluctuations at the 1.5 km scale and so on. For an original image of $N \times N$ pixels, the indices, i and j, vary from 1 to $N/2^m$ at scale m, while the primed indices, i' and j', vary from 1 to $N/2^{m+1}$. There are three normalized fluctuation components,

$$\xi_{m+1,n}(i,j) = \frac{X'_{m+1,n}(i,j)}{\overline{X}_{m+1}(i,j)}, n = 1,2,3, \qquad (2)$$

where n = 1, 2, 3, refers to the index of the directional component in the longitudinal, latitudinal, and diagonal directions, respectively. For rainfall the distributions of these normalized fluctuations are well approximated by Gaussians centered at zero [see also *Perica and Foufoula-Georgiou*, 1996b]. The distributions at each iteration may thus be fully characterized by the standard deviations, $\sigma_{\xi_{m+1,n}}$, of these distributions. Examples of the distributions of normalized fluctuations and how they change with scale are given in Figures 5a-c for an ensemble of 1 hour of Next Generation Weather Radar (NEXRAD) data at 2 km resolution. The standard deviations of the normalized fluctuations, $\sigma_{\xi_{m+1,n}}$, are a relative measure of the variability of the rainfall field at a specific scale. Small $\sigma_{\xi_{m+1,n}}$ indicates that the field mostly consists of small fluctuations relative to the intensity of the field values, while large $\sigma_{\xi_{m+1,n}}$ indicates a higher occurrence of large fluctuations relative to the intensity of the field values.

For rainfall, simple scaling is often observed in the standard deviations of the normalized fluctuations [*Perica and Foufoula-Georgiou*, 1996a; *Venugopal et al.*, 1999]. By this we mean that log-log linearity is observed on a plot of $\sigma_{\xi_{m+1,n}}$ versus scale. An example of this log-log linearity is shown in Figure 5d, where the standard deviations of the normalized fluctuations for the three fluctuation components for rainfall derived from a NEXRAD radar image at 2 km resolution are shown. The scaling observed may be expressed by

$$\sigma_{\xi_{m+1,n}} = \sigma_{\xi_{1,n}} 2^{mH_n}, n = 1,2,3, \qquad (3)$$

where H_n (determined by the slopes on the log-log plots) are the scaling exponents for each of the directional components n. H_n may be interpreted as indicators of smoothness, since a steep slope in a plot such as that shown in Figure 5d indicates a more rapid decrease in rainfall variability with decreasing scale. Equation (3) is written for the dyadic (base 2) special case, which is computationally convenient for the decomposi-

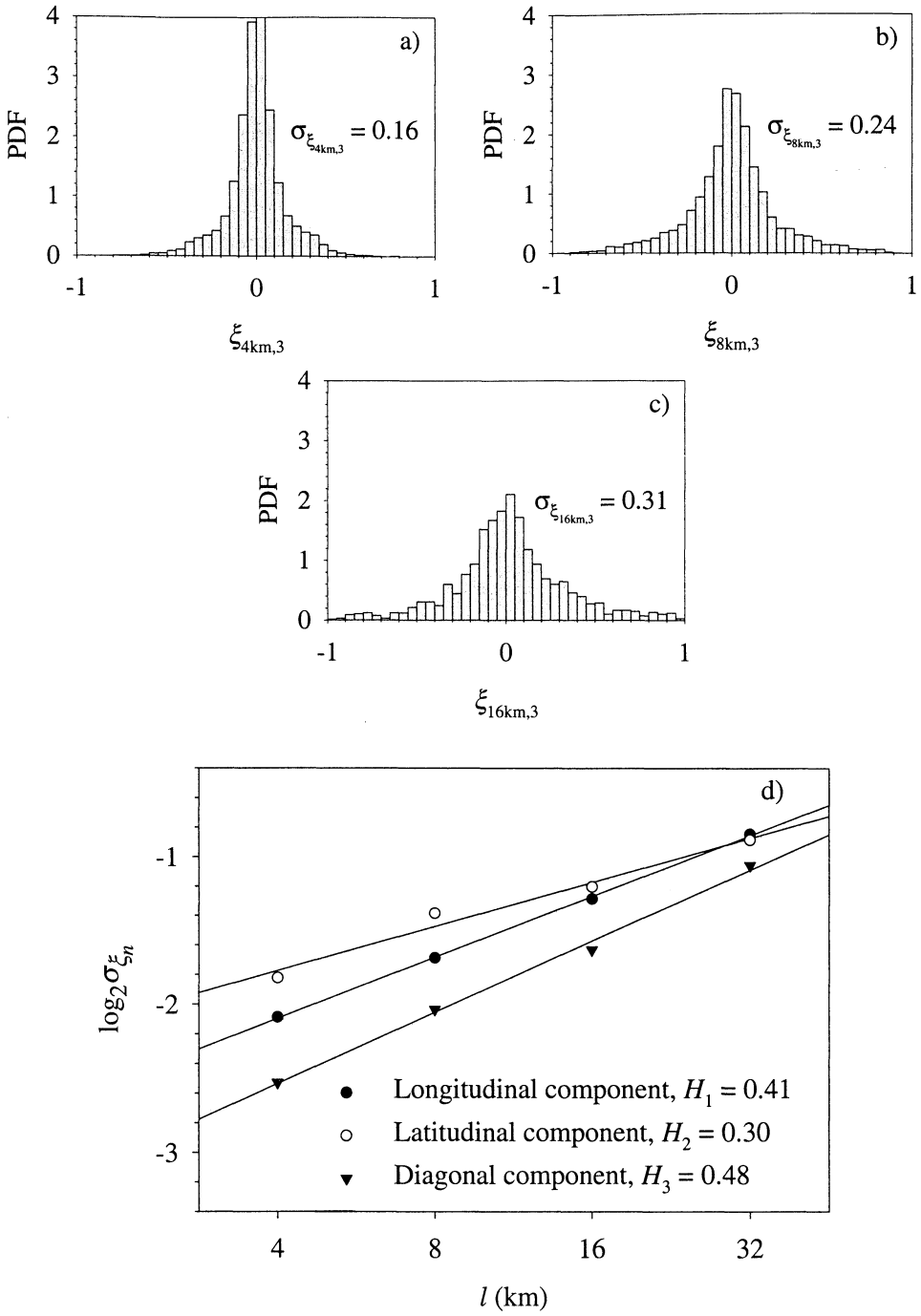

Figure 5. Probability Density Functions (PDFs) of normalized fluctuations for the diagonal component at the (a) 4 km (m = 0), (b) 8 km (m = 1), and (c) 16 km (m = 2) scales for a 1 hour ensemble of 2 km NEXRAD (KEAX) rain rate radar fields from 1000 to 1100 hours July 7, 1995, over Kansas City, Missouri. (d) Standard deviation of distributions in Figures 5a-5c are plotted versus scale on a log-log graph to yield the scaling exponents, H_n, estimated by the log-log linear slopes for each component.

tion. However, in general, it holds for any two scales, λ_1 and λ_2, in which case (3) takes on the form $\sigma_{\xi_{\lambda_2},n} = \sigma_{\xi_{\lambda_1},n}(\lambda_2/\lambda_1)^{H_n}$.

4.2. Stochastic Downscaling

Given a set of estimated parameters from relation (3) above, namely the H_n and $\sigma_{\xi_{m+1,n}}$ at any one scale, m, one can stochastically downscale a field from a coarse resolution to one of much higher resolution. The resulting field will have the same scaling properties obeying (3). *Perica and Foufoula-Georgiou* [1996b] showed how a radar image at 64 km resolution could be stochastically downscaled to 4 km resolution. The 4 km field represents a random realization that may have occurred conditional on the given 64 km averaged field. The general procedure for downscaling is described in great detail by *Perica and Foufoula-Georgiou* [1996b] and only briefly reviewed here for completeness.

As an illustration, consider the downscaling we wish to perform for this study from a scale of 3 km down to a scale of

375 m. Given the three values of H_n and three standard deviations of the normalized fluctuations at 6 km scale ($m = 4$), which is written as $\sigma_{\xi_{6km,n}} = \sigma_{4,n}$, we proceed as follows:

1. For the first pixel, (i, j), at 3 km resolution one generates three Gaussian random deviates [e.g., see *Press et al.*, 1992] with zero mean and standard deviation $\sigma = \sigma_{\xi_{3km,n}} = \sigma_{\xi_{6km,n}} 2^{-H_n}$. These three deviates are the three normalized fluctuations, $\xi_{3km,n}(i, j)$, in (2).

2. Multiplying these three variates by the pixel value at 3 km resolution, $X_{3km,n}(i, j)$, converts the three random deviates to the three absolute fluctuations, $X'_{3km,n}(i, j)$.

3. The three absolute fluctuations, $X'_{3km,n}(i, j)$, together with the mean pixel value at 3 km resolution, $X_{3km,n}(i, j)$, are transformed via the inverse Haar wavelet transform to create four pixel values at 1.5 km resolution.

4. Steps 1 through 3 are repeated for all the 3 km pixels in the image until the entire image has a 1.5 km resolution and four times as many pixels as the initial image at 3 km resolution.

5. Now steps 1 through 4 are repeated for the pixels at 1.5 km resolution but now with the Gaussian random deviates generated with $\sigma = \sigma_{\xi_{6km,n}} 2^{-2H_n}$. In the next iteration (once one has an image at 750 m resolution) the random deviates will have standard deviation $\sigma = \sigma_{\xi_{6km,n}} 2^{-3H_n}$, and so on.

A few additional minor details must be addressed in the procedure outlined above. First, the procedure allows for negative values to be generated. This occurs infrequently, but when it does, the pixel is set to zero and the four new pixels are renormalized to conserve the mean. Second, at each iterative step (i.e., after step 4 above) the four new pixels generated within each of the larger pixels from the previous step (e.g., the four new pixels at 1.5 km resolution within a single 3 km pixel) are rearranged to improve connectivity. This is done by shifting the largest intensity to the pixel that is surrounded by high intensities and the lowest intensity to the pixel surrounded by the lowest intensities [*Perica*, 1995]. This rearranging is important as the four new pixels are uncorrelated to each other and to surrounding pixels. Thus neglecting to improve the connectivity leads to a step or jump in the final spectrum of the field. In the example above, the jump would occur at a wave number of $k = (3 \text{ km})^{-1}$ (i.e., the starting scale of the downscaling procedure). An alternative method of downscaling employing the cascade-based framework of *Lovejoy and Schertzer* [1995] is currently being investigated for another study and would not require this connectivity scheme. The algorithm for the entire process of stochastic downscaling outlined above is available (in the C programming language) from the authors.

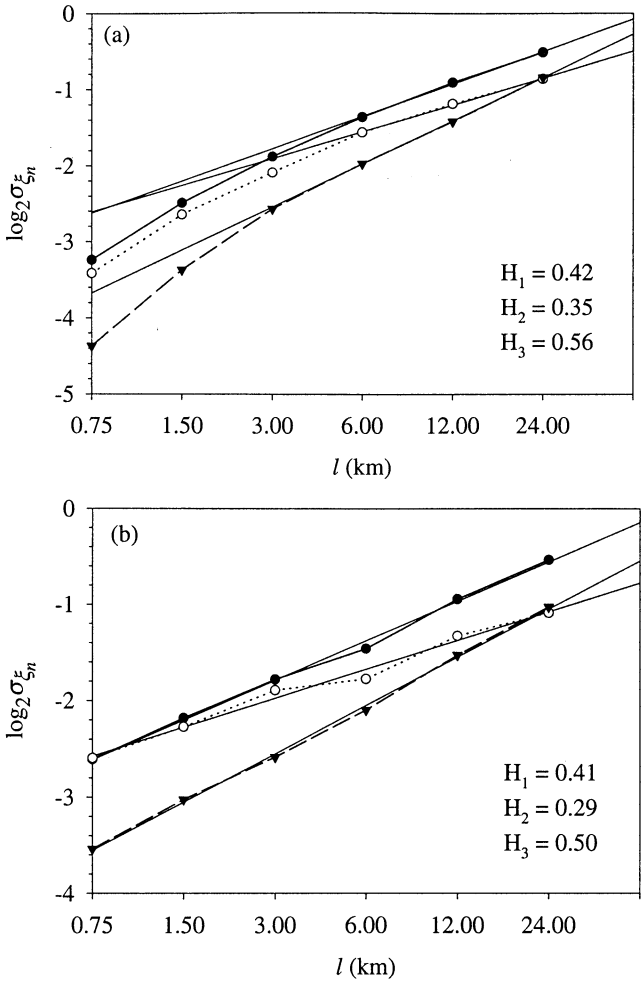

Figure 6. Log-log plots of the standard deviations of normalized fluctuations versus scale for precipitating ice at 4 km altitude from the (a) original 375 m modeled field and (b) the downscaled 375 m field. The scaling shown in Figure 6a at the largest scales (top 3 points) for each exponent yields the parameter estimates, which are used in the statistical downscaling from 3 km to 375 m (bottom 4 points in Figure 6b). Notice that the new parameter estimates in Figure 6b resulting from a regression of all 6 points differ only slightly from the parameters of Figure 6a used for the downscaling. Similar plots are obtained for the other hydrometeor fields.

5. Multiscale Statistics and Downscaling of a Numerical Cloud Model

The ARPS cloud model, as discussed in section 2, was run with a horizontal resolution of 375 m in order to explore the contribution of the variability below the 3 km scale often used in radiative transfer computations. Performing a wavelet decomposition and computation of the normalized fluctuations produces the plot shown in Figure 6a for precipitating ice at 4 km altitude. Similar plots were produced for other hydrometeor species. Scaling is observed at the larger scales above 3 km, but a rapid falloff in variability is seen to occur at smaller scales, consistent with the claims made above, that models lack small-scale variability because of such processes as computational mixing acting at scales of about 6 to 8 times the horizontal resolution of the cloud model.

Given that the model lacks variability at these smaller scales, the modeled fields were spatially averaged up to a resolution of 3 km, and using the scaling parameters retrieved from scales above 3 km (as, for example, shown in Figure 6a for precipitating ice), they were stochastically downscaled back to 375 m horizontal resolution. This therefore prescribes a scaling structure as shown in Figure 6b and effectively increases the variability at scales below 3 km in a fashion consistent with the scaling structure seen in radar observations. It is important to note that the downscaling preserves the mean of the field at each 3 km pixel and thus only acts to spatially redistribute the hydrometeors within each single 3 km pixel.

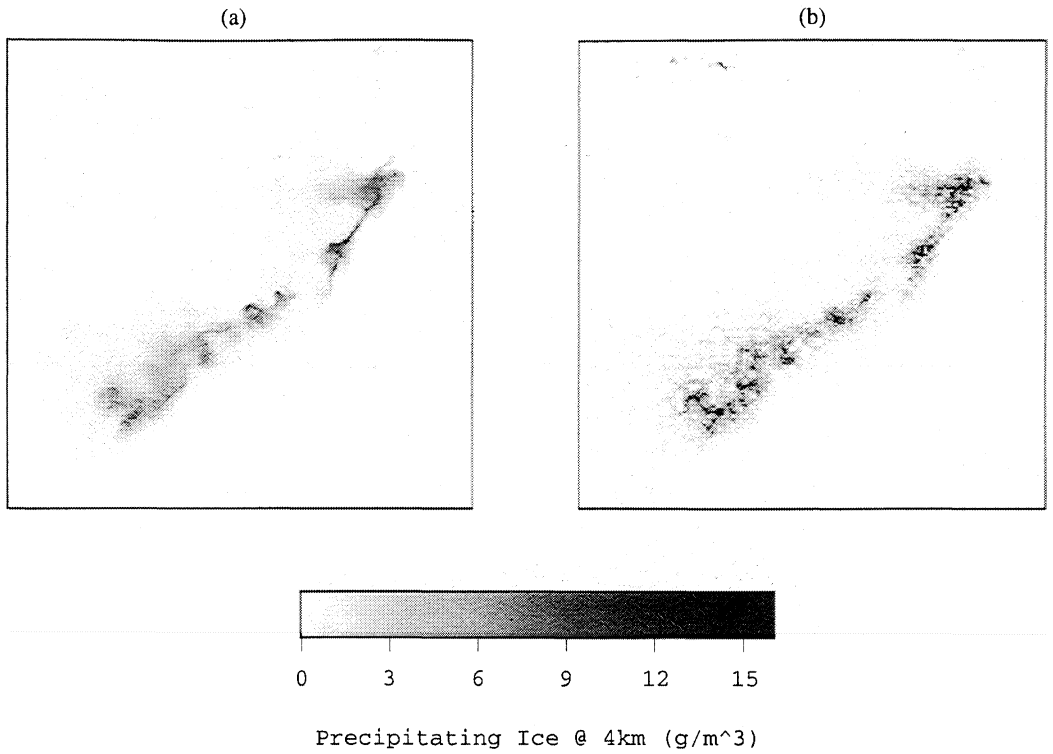

Figure 7. Downscaling process illustrated for precipitating ice (in g m^{-3}) at 4 km altitude for (a) the original 375 m modeled field, which is relatively smooth, and (b) the 375 m field created by statistically downscaling the 3 km spatially averaged field. A similar downscaling procedure was performed for all the hydrometeor species at all vertical levels for the original 375 m modeled field. The range of scales from the horizontal resolution of the cloud model (375 m) to a factor of 8 times the horizontal resolution (3 km) is the range over which numerical cloud resolving models are affected by computational mixing.

Visually, the downscaling is seen to roughen the smooth appearance of the modeled output as shown in Figure 7. The original modeled output in Figure 7a is almost smokey and laminar in appearance, uncharacteristic of precipitation viewed using radar, for example. After the downscaling the roughness is markedly increased as shown in Figure 7b.

The parameter estimation and downscaling procedure is applied to each hydrometeor species independently. The parameters used are listed in Table 1. Parameters estimated for any single hydrometeor species did not seem to vary systematically with altitude; therefore each horizontal slice in the vertical is downscaled using the same parameters. In addition, the same random seed is used for the downscaling at each individual level in the vertical. This may lead to an overestimation of the horizontal variability in the columnar integrated fields. Proper treatment requires further investigation into the vertical structure of hydrometeor concentrations and possibly 3-D downscaling techniques. However, verifications were made to show that the simplification of applying the 2-D downscaling scheme above, as opposed to a 3-D downscaling scheme, still produced realistic vertical profiles of the hydrometeor concentrations, although the vertical structure was not exactly preserved as shown in Figure 8 for precipitating ice. The mean of the four adjacent columns shown in Figure 8 represents the mean profile at a 750 m scale and is not expected to be preserved after downscaling. However, mean vertical profiles averaged to 3 km in the horizontal (i.e., the starting scale of the downscaling procedure) are necessarily preserved (exactly) by the mass conservation properties of the upscaling-downscaling procedure.

The degree to which the downscaling procedure increases variability can also be seen via a Fourier spectral analysis. Figure 9 shows the spectra for the surface rain rate before and after the downscaling. The tail in the spectrum computed

Table 1. Estimated Downscaling Parameters[a]

Hydrometeor Species	H_1	H_2	H_3	$\sigma_{\xi_{6km,1}}$	$\sigma_{\xi_{6km,2}}$	$\sigma_{\xi_{6km,3}}$
Rain	0.24	0.22	0.42	0.39	0.33	0.27
Graupel/hail	0.42	0.35	0.56	0.39	0.34	0.26
Snow	0.34	0.24	0.38	0.35	0.32	0.26
CLW[b]	0.16	0.20	0.30	0.57	0.59	0.47
CIW[c]	0.36	0.36	0.44	0.37	0.35	0.26

[a] All parameters are dimensionless (see text).
[b] CLW is cloud liquid water.
[c] CIW is cloud ice water.

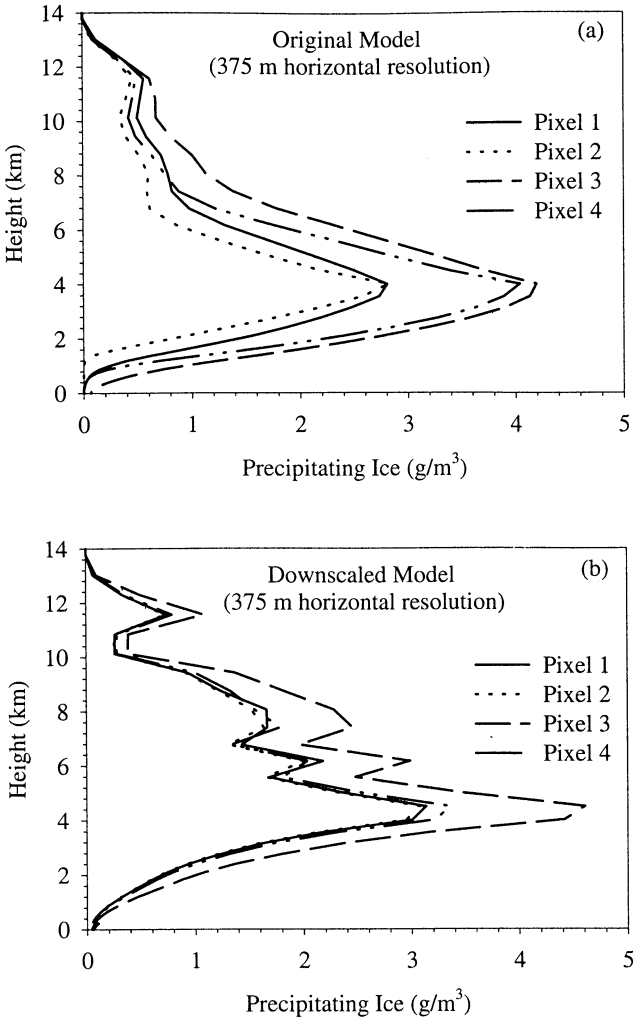

Figure 8. Vertical profiles of precipitating ice (in g m^{-3}) (a) before and (b) after applying the stochastic downscaling procedure. Profiles are shown for adjacent pixels and show that the vertical structure is not exactly preserved after the downscaling but is nonetheless a good approximation to the original modeled vertical structure. Similar results were observed for the other hydrometeor species.

from the original 375 m model is effectively raised as a result of the downscaling procedure, and scaling is observed in the power spectrum of the downscaled field. The spectral slope of the log-log linear portion of the spectrum computed from the downscaled field is –1.9. This is consistent with the lower end of the range of spectral slopes found from observed radar fields which typically lie between –1.8 and -3.0 [*Menabde et al.*, 1999; *Harris et al.*, 1998].

6. Effect of Subgrid Variability on Simulated Brightness Temperatures

As noted elsewhere in the literature [e.g., *Kummerow et al.*, 1996; *Panegrossi et al.*, 1998; *Haferman et al.*, 1994], the scale at which one performs the radiative transfer scheme affects the simulated brightness temperatures. Capitalizing on a very high resolution run of 375 m in the horizontal, the effect of the scale at which the radiative transfer is performed is investigated by simply varying the resolution of the hydrometeor fields through spatial averaging. At each scale the radiative transfer scheme is applied and the comparison is made at 12 km by averaging the brightness temperature fields (i.e., the results of a 3 km radiative transfer are averaged by a factor of 4 and those of a 375 m radiative transfer are averaged by a factor of 32). A scale of 12 km corresponds roughly to the highest TMI resolution.

Following the terminology used by *Roberti et al.* [1994], comparisons are made by computing the mean (absolute) deviation, Δ, found by taking the mean of the absolute differences in brightness temperatures over the field,

$$\Delta = \frac{1}{N}\sum_{i=1}^{N} \left|\mathbf{T}_{\mathbf{b},\text{field 1}} - \mathbf{T}_{\mathbf{b},\text{field 2}}\right|, \tag{4}$$

where i is an index representing the 12 km pixels and N is the number of pixels. The number of pixels, N, was chosen either to be all the (12 km) pixels in a field or, only the pixels for which it was raining at the ground. The latter gives a more meaningful measure of the mean deviation, since much of the domain is not precipitating and void of ice and liquid water. Mean deviations were computed comparing the downscaled 375 m fields with the 3 km fields, the original (undownscaled) 375 m fields with the 3 km fields, as well as the downscaled 375 m fields with the original 375 m fields. Biases, B, were also computed for the entire regions and rainy regions of the modeled fields, using the same relation as (4) but without the absolute value,

$$B = \frac{1}{N}\sum_{i=1}^{N} \left(\mathbf{T}_{\mathbf{b},\text{field 1}} - \mathbf{T}_{\mathbf{b},\text{field 2}}\right) \tag{5}$$

The mean deviations and biases are summarized in Table 2 for the 10.7 GHz, 19 GHz, 37 GHz, and 85.6 GHz horizontally polarized channels, with values in parentheses for the entire domain, while the remaining values are for the raining pixels only. Table 2 shows three comparisons. The first of

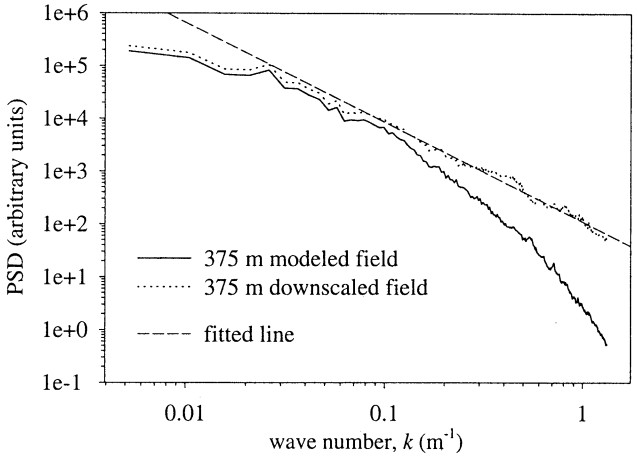

Figure 9. Fourier power spectra for surface rain rate from the 375 m field before (solid line) and after (dotted line) downscaling. Comparison of the two spectra illustrates how downscaling increases variability for the scales ranging from the horizontal resolution of the field (375 m) to 8 times the resolution of the field (3 km). The regression fit (dashed line) to the spectrum of the downscaled field has a slope of –1.9 and indicates how the downscaling prescribes a scaling structure often seen in cloud and precipitation fields (see text).

Table 2. Mean Absolute Deviations and Biases[a]

	Comparison 1 $T_{b,375\ m} - T_{b,3km}$		Comparison 2 $T_{b,down} - T_{b,3\ km}$		Comparison 3 $T_{b,down} - T_{b,375\ m}$	
Channel	Mean Deviation Δ, °K	Bias B, °K	Mean Deviation Δ, °K	Bias B, °K	Mean Deviation Δ, °K	Bias B, °K
10.7 GHz	1.06 (0.460)	-0.993 (-0.430)	2.38 (1.04)	-1.88 (-0.811)	1.31 (0.604)	-0.836 (-0.381)
19.3 GHz	0.807 (0.359)	-0.792 (-0.349)	2.46 (1.09)	-2.38 (-1.04)	1.65 (0.765)	-1.51 (-0.694)
37.0 GHz	0.848 (0.411)	-0.576 (-0.292)	2.33 (1.09)	-1.73 (-0.825)	1.87 (0.886)	-1.11 (-0.532)
85.6 GHz	1.67 (0.837)	+1.37 (+0.641)	5.55 (2.71)	+4.99 (+2.39)	5.01 (2.43)	+3.58 (+1.75)

[a] Δ is from Equation (4) and B is from equation (5) in $T_{b,sim}$ at the 12 km scale between resulting radiative transfers computed for comparison 1, original modeled 375m and 3 km; comparison 2, downscaled 375 m field and 3 km; and comparison 3, downscaled 375 m and original modeled 375 m. Values in parentheses are for the entire domain, while other values are for the pixels for which it is raining on the ground.

the three comparisons is between the 375 m original modeled fields and the 3 km fields (spatially averaged hydrometeors) and represents the mean deviations and biases that arise from ignoring the originally modeled variability at scales below 3 km. The biases and mean deviations are small and suggest that not much is gained by modeling down to 375 m. The second comparison is between the 375 m downscaled modeled fields and the 3 km fields and represents the difference in $T_{b,sim}$ fields when the subgrid variability at scales below 3 km is realistic. The biases and mean deviations in this second comparison are far greater and are similar in magnitude to the biases and mean deviations found when comparing 3-D radiative transfer results with Independent Column Approximation results as documented by *Roberti et al.* [1994]. This suggests that the underrepresentation of hydrometeor variability in the cloud model at scales below 3 km may have a profound influence on simulated brightness temperatures. In fact, the third comparison in Table 2, between the downscaled and original 375 m fields, is representative of the effect of the downscaling alone and exceeds the effect of ignoring the originally modeled subgrid variability between 3 km and 375 m.

An additional presentation of the findings is provided by scatterplots of the bias at each 12 km pixel in the second comparison of Table 2 (between the 375 m downscaled modeled fields and the 3 km fields) versus $T_{b,sim}$ from the downscaled fields and are shown in Figure 10 for the 10.7 GHz, 19 GHz, 37 GHz, and 85.6 GHz horizontally polarized channels. Each point in the scatterplots represents the difference between the brightness temperature of a 12 km pixel of the downscaled field and the corresponding 12 km pixel in the 3 km field. These scatterplots illustrate the distribution and maximum biases between the downscaled (375 m) and 3 km fields at the 12 km scale. The areas of greatest density in the scatterplots are near the horizontal line of zero difference and are for pixels representative of the background atmosphere (largely void of ice and water) as subgrid variability has little effect on these regions of the cloud model domain. All plots show a decrease in bias with increase in $T_{b,sim}$, with maximum biases of approximately -17°K for the 10.7, 19, and 37 GHz horizontally polarized channels and approximately +17°K for the 85.6 GHz horizontally polarized channel. Again, the magnitudes of the differences are comparable with 3-D to plane-parallel differences found for similar plots by *Haferman et al.* [1994], particularly for the lower frequencies. Furthermore, on the basis of the results of *Haferman et al.* [1994], which show the same (downward sloping) trends in the biases between 3-D and plane-parallel schemes, it is argued that one could also hypothesize that if a 3-D radiative transfer were performed on the fields used in this study, the same trends in the scatterplots would continue to exist. In particular, for the 85.6 GHz channel where scattering effects are dominant, the magnitudes of the deviations would be increased.

7. Concluding Remarks

The study performed here concerns the simulation of upwelling brightness temperatures in a numerical cloud model for the purpose of rainfall estimation from microwave sensors. The study is largely illustrative in nature and investigates the simple questions as to (1) whether subgrid variability is even worth modeling, (2) whether it is important to worry about reduced variability of modeled hydrometeor concentrations, and (3) whether it is feasible to apply a stochastic downscaling procedure to correct for the reduced variability at modeled grid scales and also to enhance the subgrid variability. The results suggest significant differences in simulated brightness temperature when subgrid variability is included and even more significant differences (more than double) when the variability is enhanced using stochastic downscaling. However, before the results can have a practical application in the inversion algorithms for rainfall estimation, a number of extensions to this study need to be investigated. First, this study used a simple Independent Column Approximation for the radiative transfer, whereas questions pertaining to scale issues associated with the spatial structure of precipitation fields can be more accurately addressed using a 3-D radiative transfer scheme [*Roberti et al.*, 1994; *Haferman et al.*, 1994; *Roberti and Kummerow*, 1999]. The use of an Independent Column Approximation radiative transfer scheme represents a first-order approximation to estimating biases occurring only from the non-uniform beam-filling (or non-linear averaging) problem. Use of a 3-D radiative transfer scheme accounts for other effects in addition to the non-linear averaging problem such as the interaction of radiation with neighboring columns and energy leakage (horizontally) from dense areas to surrounding areas [*Liu et al.*, 1996; *Roberti et al.*, 1994]. Use of 3-D radiative transfer schemes may thus result in even greater biases than those found in this study, but this needs to be properly quantified. Also, as already discussed, this needs to be accompanied by greater attention to stochastic downscaling in three dimensions. In this study, only a 2-D isotropic stochastic downscaling procedure was implemented, although examination of the vertical profiles of hydrometeor concentrations after implementing the downscaling showed a reasonably realistic vertical structure of hydrometeor concentrations. Three-dimensional downscaling techniques are more complex as they require proper treatment of anisotropy (i.e., the vertical structure is vastly different from the horizontal

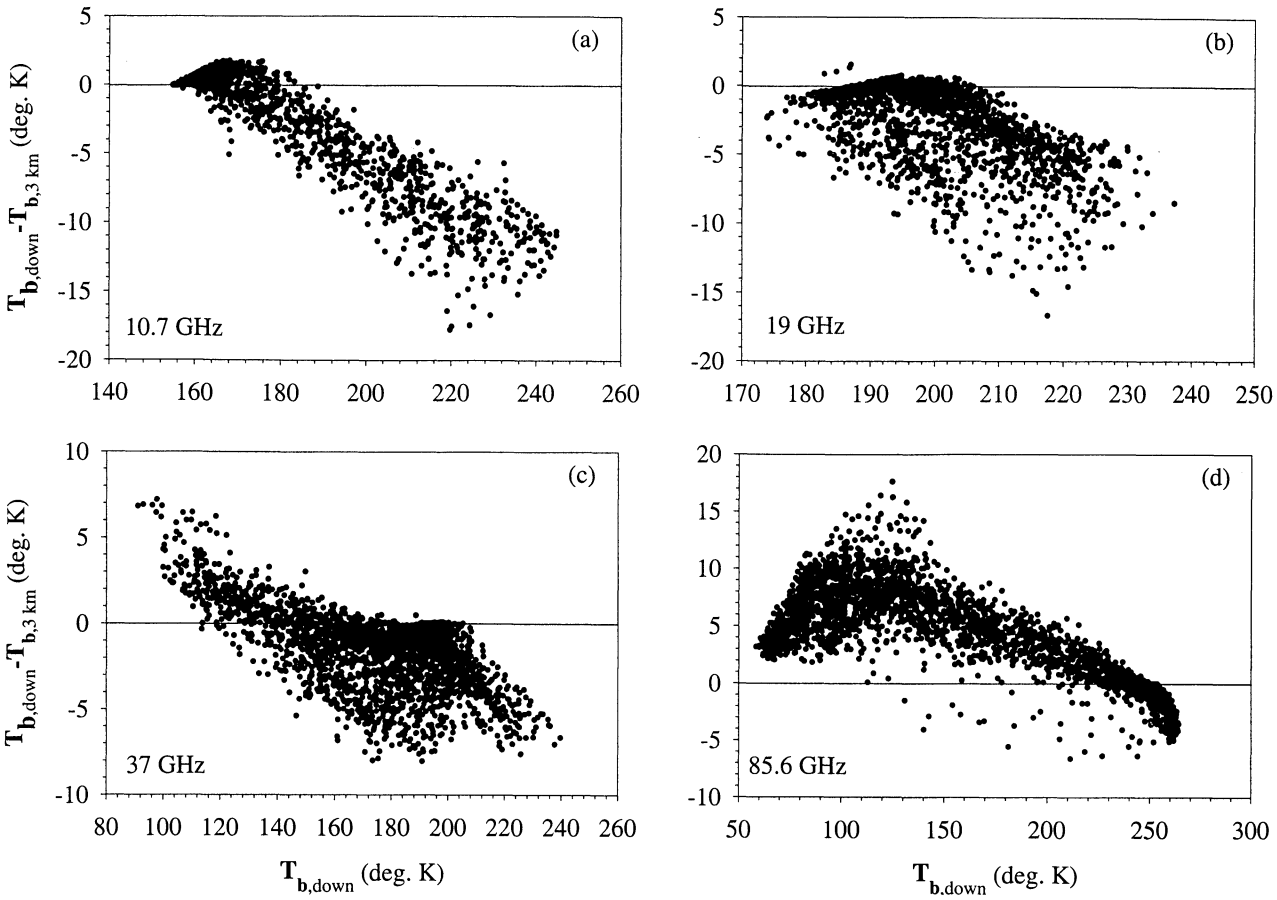

Figure 10. Scatterplots of the pixel-by-pixel differences in simulated brightness temperature (compared at the scale of 12 km) between radiative transfer results for the 375 m downscaled fields and the 3 km fields.

structure), whereas the 2-D horizontal structure of precipitation at scales between 3 km and 375 m is nearly isotropic, and thus isotropic downscaling is adequate.

Another logical extension requiring greater computer resources involves stochastically downscaling the modeled fields down to even smaller scales of, say, 50 m. Extra computer resources would only be required to perform the radiative transfer over such a fine scale and are thus still feasible. Any radiative transfer scheme used for a field with such a small horizontal gridsize would have to be a 3-D scheme, as the absorption mean free paths of the photons would be many times larger than the horizontal inhomogeneities of the cloud model [*Roberti et al.*, 1994]. Running a cloud model itself at such a resolution over a comparable domain (large domains are necessary since the TMI sensors are of the order of 10 km in resolution; a 100 km long squall line, for example, is only 10 TMI pixels long) would be incredibly expensive if not infeasible. It is therefore apparent that the recent advent of stochastic downscaling procedures and their application to problems involving subgrid variability becomes a powerful tool for exploring questions related to the importance of subgrid variability in satellite rainfall estimation even when the scales of practical interest are much larger than these subgrid scales.

Clearly one of the questions regarding the pertinence of these results is the validity of the scaling structure imposed by the downscaling procedure. While plenty of evidence exists to suggest that scaling is a statistical property of observed precipitation and cloud fields, higher-resolution measurements of precipitation would strengthen the assertion that scaling is present to scales of a few hundred meters. A very high resolution study of the 3-D structure of snow fields using stereo photogrammetry [*Lovejoy et al.*, 1999] suggests the presence of scaling down to centimeter scales, although modeling variability to such extremely fine scales may not be necessary for microwave applications. New observations recently obtained at a number of TRMM validation field projects such as the Large Scale Biosphere-Atmosphere Experiment (LBA), TEFLUN, and Kwajalein Experiment (KWAJEX) should provide valuable data sets to answer these questions. Furthermore, the parameters used in the downscaling (see Table 1) are representative of a convective squall line. Extending this study to include stratiform as well as other convective systems would provide useful results as stratiform precipitating clouds are radiometrically very different from convective systems owing to differences in their vertical structure. On the basis of studies such as that of *Harris et al.* [1996], the scaling structure and therefore the downscaling parameters would also differ greatly for stratiform precipitation.

A final note concerns the comparison of the 3 km aggregated field (obtained by upscaling the 375 m modeled field) to a field from a model run at 3 km resolution. An important difference is that a field from a model run at 3 km will have reduced variability at scales from 3 km to maybe as high as 18-24 km, whereas the spatially aggregated field used here

does not suffer from this. This means that the biases reported here may, in fact, be underestimating the biases that would result by including subgrid variability in the rainfall estimation algorithms based on the typical cloud model runs at 1-3 km resolution. How much of an underestimation, however, is difficult to determine. A model run at 3 km resolution and simulated with identical initial conditions as the 375 m model (except for the spatial resolution, corresponding temporal integration time and computational mixing [see *Droegemeier et al.*, 1994]) produces a storm very similar to the 375 m model. However, while the surface rainfall was approximately the same for both runs, the precipitating ice content aloft was not the same. Because of this problem a straightforward comparison of a 3 km run with the 375 m run was not feasible. This issue points to the importance of studying in greater detail the effects of scale and computational mixing on probability distributions of the modeled hydrometeors, as these are central to any study addressing issues of rainfall estimation from space.

Appendix A: Fourier Spectral Analysis

The Fourier transform of an image may be approximated with a 2-D FFT [*Press et al.*, 1992] and can be computed for any 2-D horizontal slice of a hydrometeor field such as RLW from the modeled atmosphere. By multiplying the 2-D FFT by its complex conjugate one obtains the 2-D energy spectrum, $E(k_x, k_y)$ of the image, where k_x and k_y are the wave number components. To facilitate visualization and comparison, the 2-D power spectra from the fields are averaged angularly about $k_x = k_y = 0$ to yield what is referred to here as the isotropic energy spectrum, $E(k)$ with $k = (k_x^2+k_y^2)^{1/2}$. We found it useful to reorder the FFT vector of *Press et al.* [1992] by centering $k_x = k_y = 0$, in order to facilitate the angular averaging. The term isotropic energy spectrum is not to suggest that the fields are isotropic but rather that the angular averaging about $k_x = k_y = 0$ integrates the anisotropy facilitating visual comparison.

Acknowledgments. This work has been supported by the NASA-TRMM program (grant NAG5-7715) and partially by the U.S. Weather Research Program (under NSF grant ATM-9714387) and the NOAA/NASA-GCIP (under grant NAG8-1519). We wish to thank Chris Kummerow for invaluable discussions and for providing the Eddington Approximation Radiative Transfer code. We also wish to thank the scientists at the Center for the Analysis and Prediction of Storms (CAPS), University of Oklahoma, for their support in our modeling efforts with the Advanced Regional Prediction System (ARPS). Finally, we wish to thank the University of Minnesota Supercomputing Institute without whose resources and technical assistance this project would not be possible.

References

Daubechies, I., *Ten Lectures on Wavelets*, Soc. For Appl. and Ind. Math., Philadelphia, Pa., 1992.

Davis, A., A. Marshak, W. Wiscombe, and R. Cahalan, Scale invariance of liquid water distributions in marine stratocumulus, part I, Spectral properties and stationarity issues, *J. Atmos. Sci.*, *53*, 1538-1558, 1996.

Droegemeier, K. K., S. M. Lazarus, and R. Davies-Jones, The influence of helicity on numerically simulated convective storms, *Mon. Weather Rev.*, *121*, 2005-2029, 1993.

Droegemeier, K. K., G. Bassett, and M. Xue, Very high resolution, uniform-grid simulations of deep convection on a massively parallel processor: Implications for small-scale predictability, paper presented at 10th Conference on Numerical Weather Prediction, Am. Meteorol. Soc., Portland, Oreg., 1994.

Farrar, M.R., E. A. Smith, and X. Xiang, The impact of spatial resolution enhancement of SSM/I microwave brightness temperatures on rainfall retrieval algorithms, *J. Appl. Meteorol.*, *33*, 313-333, 1994.

Foufoula-Georgiou, E., and P. Kumar (Eds.), *Wavelets in Geophysics*, Academic, San Diego, Calif., 1994.

Georgakakos, K. P., A. A. Carsteanu, P. L. Sturdevant, and J. A. Cramer, Observation and analysis of midwestern rain rates, *J. Appl. Meteorol.*, *33*, 1433-1444, 1994.

Haferman, J. L., W. F. Krajewski, and T. F. Smith, Three-dimensional aspects of radiative transfer in remote sensing of precipitation: The 1986-COHMEX Storm, *J. Appl. Meteorol.*, *33*, 1609-1622, 1994.

Harris, D., M. Menabde, A. Seed, and G. L. Austin, Multifractal characterization of rain fields with a strong orographic influence, *J. Geophys. Res.*, *101*(21), 26,405-26,414, 1996.

Harris, D., M. Menabde, and G. L. Austin, Breakdown coefficients and classification by scaling properties of rain fields, paper presented at 6th International Conference on Precipitation, NSF, NASA/NOAA, Mauna Lani Bay, Hawaii, June 29 to July 1, 1998.

Kumar, P., and E. Foufoula-Georgiou, A multicomponent decomposition of spatial rainfall fields, 1, Segregation of large and small-scale features using wavelet transforms, *Water Resour. Res.*, *28*, 2515-2544, 1993a.

Kumar, P., and E. Foufoula-Georgiou, A multicomponent decomposition of spatial rainfall fields, 2, Self-similarity in fluctuations, *Water Resour. Res.*, *28*, 2515-2544, 1993b.

Kummerow, C., On the accuracy of the Eddington approximation for radiative transfer in the microwave frequencies, *J. Geophys. Res.*, *98*(2), 2757-2765, 1993.

Kummerow, C., Beamfilling errors in passive microwave rainfall retrievals, *J. Appl. Meteorol.*, *37*, 356-370, 1998.

Kummerow, C., and L. Giglio, A passive microwave technique for estimating rainfall and vertical structure information from space, part I, Algorithm description, *J. Appl. Meteorol.*, *33*, 3-18, 1994.

Kummerow, C., W. S. Olson, and L. Giglio, A simplified scheme for obtaining precipitation and vertical hydrometeor profiles from passive microwave sensors, *IEEE Trans. Geosci. Remote Sens.*, *34*(5), 1213-1232, 1996.

Kummerow, C., W. Barnes, T. Kozu, J. Shiue, and J. Simpson, The Tropical Rainfall Measuring Mission (TRMM) sensor package, *J. Atmos. Oceanic Tech.*, *15*(3), 809-817, 1998.

Lin, Y., R. D. Farley, and H. D. Orville, Bulk parameterization of the snow field in a cloud model, *J. Appl. Meteorl.*, *22*, 1065-1092, 1983.

Liu, Q., C. Simmer, and E. Ruprecht, Three-dimensional radiative transfer effects of clouds in the microwave spectral range, *J. Geophys. Res.*, *101*(2), 4289-4298, 1996.

Lovejoy, S., and D. Schertzer, Multifractals and rain, in *New Uncertainty Concepts in Hydrology and Water Resources*, edited by A. W. Kundzewicz, pp. 61-103, Cambridge Univ. Press, New York, 1995.

Lovejoy, S., N. Desaulniers-Soucy, and D. Schertzer, Empirical analysis of the continuum limit in rain (abstract), *Eos Trans. AGU, 80*(46), Fall Meet. Suppl., F438, 1999.

Menabde, M., A. W. Seed, D. Harris, and G. L. Austin, Self-similar random fields and rainfall simulation, *J. Geophys. Res.*, *102*(12), 13,509-13,515, 1997.

Menabde, M., A. Seed, D. Harris, and G. Austin, Multiaffine random field model of rainfall, *Water Resour. Res.*, *35*, 509-514, 1999.

Mugnai, A., E. A. Smith, and G. J. Tripoli, Foundations for physical-statistical precipitation retrieval from passive microwave satellite measurements, Part II, Emission source and generalized weighting function properties of a time dependent cloud-radiation model, *J. Appl. Meteorol.*, *32*, 17-39, 1993.

Panegrossi, G., S. Dietrich, F. S. Marzano, A. Mugnai, E. A. Smith, X. Xiang, G. J. Tripoli, P. K. Wang, and J. P. V. P. Baptista, Use of cloud model microphysics for passive microwave-based precipitation retrieval: Significance of consistency between model and measurement manifolds, *J. Atmos. Sci.*, *55*, 1644-1672, 1998.

Perica, S., A model for multiscale disaggregation of spatial rainfall based on coupling meteorological and scaling descriptions, Ph.D. thesis, Univ. of Minn., Minneapolis, 1995.

Perica, S., and E. Foufoula-Georgiou, Linkage of scaling and thermodynamic parameters in rainfall: Results from midlatitude

mesoscale convective systems, *J. Geophys. Res.*, *101*(3), 7431-7448, 1996a.

Perica, S., and E. Foufoula-Georgiou, A model for multiscale disaggregation of spatial rainfall based on coupling meteorological and scaling descriptions, *J. Geophys. Res.*, *101*(21), 26,347-26,361, 1996b.

Pielke, R. A., *Mesoscale Meteorological Modeling*, Academic, San Diego, Calif., 612 pp., 1984.

Porté-Agel, F., C. Meneveau, and M. B. Parlange, A scale-dependent dynamic model for large-eddy simulation: Application to a neutral atmospheric boundary layer, *J. Fluid Mech.*, *415*, 261-284, 2000.

Porté-Agel, F., M. B. Parlange, C. Meneveau, and W. E. Eichinger, A priori field study of the subgrid-scale heat fluxes and dissipation in the atmospheric surface layer, *J. Atmos. Sci.*, in press, 2001.

Press, W. H., S. A. Teukolsky, W. T. Vetterling, and B. P. Flannery, *Numerical Recipes in C: The Art of Scientific Computing,* 2nd ed., 994 pp., Cambridge Univ. Press, New York, 1992.

Roberti, L., and C. Kummerow, Monte Carlo calculations of polarized microwave radiation emerging from cloud structures, *J. Geophys. Res.*, *104*(2), 2093-2104, 1999.

Roberti, L., J. Haferman, and C. Kummerow, Microwave radiative transfer through horizontally inhomogeneous precipitating clouds, *J. Geophys. Res.*, *99*(8), 16,707-16,718, 1994.

Schertzer, D., and S. Lovejoy, Non-linear geodynamical variability: Multiple singularities, universality and observables, in *Scaling, Fractals and Non-linear Variability in Geophysics*, edited by D. Schertzer and S. Lovejoy, pp. 41-82, Kluwer, Netherlands, 1991.

Seed, A.W., J. Nicol, G.L. Austin, S.G. Bradley and C.D. Stow, The impact of radar and raingauge sampling errors when calibrating a weather radar, *Meteorol. Appl.*, *3*, 43-52, 1996.

Simpson, J., C. Kummerow, W.–K. Tao, and R. F. Adler, On the Tropical Rainfall Measuring Mission (TRMM), *Meteorol. Atmos. Phys.*, *60*, 19-36, 1996.

Smith, E. A., X. Xiang, A. Mugnai, and G. J. Tripoli, Design of an inversion-based precipitation profile retrieval algorithm using an explicit cloud model for initial guess microphysics, *Meteorol. Atmos. Phys.*, *54*, 53-78, 1994.

Spencer, R. W., A satellite passive 37-GHz scattering-based method for measuring oceanic rain rates, *J. Appl. Meteorol.*, *25*(6), 754-766, 1986.

Stephens, G. L., Radiative transfer through arbitrarily shaped optical media, part II, Group theory and simple closures, *J. Atmos. Sci.*, *45*, 1837-1848, 1989.

Tao, W., and J. Simpson, Goddard cumulus ensemble model, part I, Model description, *TAO*, *43*, 35-72, 1993.

Venugopal, V., E. Foufoula-Georgiou, and V. Sapozhnikov, A space-time downscaling model for rainfall, *J. Geophys. Res.*, *104*(16), 705-721, 1999.

Weisman, M. L., and J. B. Klemp, The dependency of numerically simulated convective storms on vertical wind shear and buoyancy, *Mon. Weather Rev.*, *110*, 504-520, 1982.

Xue, M., K. K. Droegemeier, V. Wong, A. Shapiro, and K. Brewster, Advanced Regional Prediction System (ARPS), version 4.0 user's guide, Cent. for Anal. and Predict. of Storms (CAPS), Univ. of Oklah., Norman, 1995.

E. Foufoula-Georgiou and D. Harris, St. Anthony Falls Laboratory, University of Minnesota, Mississippi River at 3rd Ave., S.E., Minneapolis, MN 55414. (efi@tc.umn.edu)

(Received February 9, 2000; revised October 16, 2000;
accepted October 19, 2000.)